Journal of The Electrochemical Society, **163** (13) F1433-F1439 (2016)
0013-4651/2016/163(13)/F1433/7/$33.00 © The Electrochemical Society

High-Pressure Performance of Mixed-Conducting Oxygen Electrodes: Effect of Interstitial versus Vacancy Conductivity

Justin Railsback,[a,*,z] Gareth Hughes,[a] Liliana Mogni,[b] Alejandra Montenegro-Hernández,[b] and Scott Barnett[a,]**

[a]*Department of Materials Science and Engineering, Northwestern University, Evanston, Illinois 60208, USA*
[b]*Consejo Nacional de Investigaciones Cientificas y Tecnicas (CONICET)-Comision Nacional de Energia Atomica (CNEA), Centro Atomico Bariloche, Bariloche CP8400, Argentina*

Electrochemical response was measured as a function of oxygen pressure pO_2 up to 10 bar for four different mixed-conducting oxygen electrode materials, the oxygen-vacancy-conducting perovskites $(Sm_{0.5}Sr_{0.5})CoO_3$ (SSC) and $(La_{0.6}Sr_{0.4})(Co_{0.2}Fe_{0.8})O_3$ (LSCF), and the interstitial-oxygen-conducting nickelates Pr_2NiO_4 (PNO) and Nd_2NiO_4 (NNO). The impedance spectroscopy (IS) measurements were done on symmetrical cells with either single-phase or two-phase infiltrated electrode structures. The polarization resistance decreased with increasing pressure in all cases, but the nickelates decreased more rapidly than the perovskites. It is proposed that this difference is a direct result of the different pO_2 dependences of the defect concentrations – the oxygen vacancy concentration decreases with increasing pO_2, whereas interstitial concentrations increase. In order to test this hypothesis, point defect concentrations were calculated for LSCF and NNO single-phase electrodes using the Adler-Lane-Steele model from electrochemical data and electrode microstructural parameters obtained by three-dimensional tomography. The results verified that the observed changes with increasing pO_2 can be explained by reasonable decreases in LSCF vacancy concentration and increases in NNO interstitial concentration. These results suggest that nickelate electrodes can be advantageous for pressurized devices.

Manuscript submitted August 11, 2016; revised manuscript received September 27, 2016. Published October 6, 2016.

The pressurized operation of solid oxide cells (SOCs) has been proposed and investigated as a means to improve cell performance,[1-3] to better interface with a downstream process or to alter reaction products.[4,5] For example, solid oxide fuel cell – turbine hybrid systems are generally designed to operate at elevated pressure.[3,6–8] Solid oxide electrolysis cells can be pressurized so that cell products can be easily introduced into pressurized catalytic reactors.[1,9] Recently, reversible SOCs have been proposed as the basis for a new electrical energy storage technology; however, achieving round-trip efficiencies >70% requires cell operation under pressurized conditions, and preferably at low temperature (<600°C).[4,5,10,11]

There have been a few reports describing the performance of SOFCs at high pressures,[1,3,12–14] but few examples where the pressure dependent electrochemical characteristics of an individual SOC electrode has been characterized.[15] There are no reports, to our knowledge, showing the effect of pressurization on mixed ionically and electronically conducting (MIEC) electrodes, which are typically used as the oxygen electrodes in low-temperature SOCs.[16] Understanding MIEC electrochemical characteristics at high pressure is important for predicting how pressurized SOC stacks will perform. Furthermore, it is useful to identify specific materials that yield low oxygen electrode resistance under pressurization, especially since oxygen electrodes are typically a primary factor limiting SOC performance, at low temperature.[16]

Here we report new results on the electrochemical characteristics of several promising low temperature MIEC electrode materials under pressurized conditions: two oxygen-ion vacancy conducting MIECs, $(Sm_{0.5}Sr_{0.5})CoO_{3-\delta}$ (SSC) and $(La_{0.6}Sr_{0.4})(Co_{0.2}Fe_{0.8})O_{3-\delta}$ (LSCF), and two oxygen-interstitial conducting MIECs, $Nd_2NiO_{4+\delta}$ (NNO), and $Pr_2NiO_{4+\delta}$ (PNO). The SSC and PNO electrodes were made by infiltration into ionic-conductor scaffolds, whereas the LSCF and NNO electrodes were made by conventional powder processing methods. In all cases, the interstitial-conducting MIECs show a larger decrease in polarization resistance with increasing oxygen pressure pO_2 than the vacancy conductors. It is proposed that increasing pO_2 improves defect transport kinetics in nickelate electrodes due to an increasing interstitial concentration, whereas defect transport kinetics in perovskite electrodes are degraded by decreasing vacancy concentration. This hypothesis is tested by manipulating the Adler-Lane-Steele (ALS) model in order to calculate pressure-dependent point defect concentrations in LSCF[17] and NNO[18] electrodes, utilizing measured electrochemical characteristics and 3D tomographic microstructural data.

*Electrochemical Society Student Member.
**Electrochemical Society Member.
[z]E-mail: justinrailsback2016@u.northwestern.edu

Experimental

Four different types of symmetrical cells were prepared and electrochemically tested versus pO_2. Two of the cells had infiltrated electrodes, (1) PNO infiltrated into LSGM scaffolds with LSGM electrolyte, and (2) SSC infiltrated into GDC scaffolds with GDC electrolyte. Two of the cells had powder-processed single-phase porous electrodes, (3) NNO on LSGM electrolyte and (4) LSCF on GDC electrolyte.

Single phase LSCF symmetric cell fabrication.—The cell fabrication method is similar to that described in Ref. 19. Briefly, gadolinium doped ceria (Rhodia) was ball milled in ethanol for 24 hours, dried, and pressed into 19 mm diameter 0.4 g pellets without binder. These pellets were fired at 1450°C for 6 hours and served as the electrolyte support for symmetric LSCF electrodes. The LSCF (Praxair) was three-roll milled with Heraeus-V737 organic vehicle in a 1:1.17 mass ratio to form an LSCF ink. The LSCF ink was screen printed onto the sintered pellets and fired at 1100°C for 1 hour resulting in a ∼20 μm thick electrode. Silver metal grids were applied as current collectors for electrochemical testing.

Single phase NNO symmetric cell fabrication.—The cell fabrication method is similar to that described in Ref. 20. Briefly, commercial LSGM (Fuel Cell Materials) was pressed to 19 mm diameter pellets and sintered at 1500°C for 4 hours to form the electrolyte support for the NNO symmetrical cells. NNO powders were synthesized by a sol-gel route.[21] Nd_2O_3 and $Ni(CH_3COO)_3 \cdot H_2O$ were dissolved with acetic acid, hexamethylenetetramine (HMTA) and acetylacetone, using a ligand to metal molar ratio of 3:1. This solution was heated to gel and then fired at 400°C and calcined at 950°C for 12 hours. The resultant NNO powder was suspended with polyvinyl butyral (2wt%), polyethyleneglycol (1 wt%), ethanol (30 wt%) and α-terpineol (27 wt%), which were then deposited onto the LSGM pellets by spin coating. These electrodes were dried and fired at 1000°C for 1 hour resulting in a final thickness of ∼10 μm. Gold metal grids were applied as current collectors for electrochemical testing.

SSC infiltrated GDC symmetric cell fabrication.—The cell fabrication method is similar to that described in Ref. 22. Briefly, pellets of GDC were fabricated as above to serve as electrolyte supports. For the GDC scaffold inks, the GDC (Rhodia) powder was three-roll

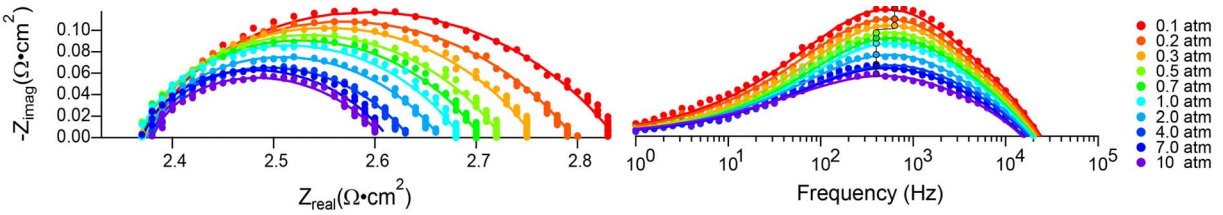

Figure 1. Nyquist and Bode plots as a function of oxygen pressure at 550°C for $(Sm_{0.5}Sr_{0.5})CoO_3$ infiltrated into GDC. The resistance values are taken from fits using a general (L-R-RQ) circuit. Fits are displayed as solid lines on the plots and the maximum frequency is outlined on the Bode plot.

milled with Heraeus-V737 organic vehicle to form a 7.31 vol% GDC ink. The GDC ink was screen printed onto the sintered pellets and fired at 1100°C for 4 hours with a final scaffold thickness of ∼20 μm. The SSC infiltrate solution was prepared by dissolving $Sm(NO_3)_3 \cdot 6H_2O$, $Sr(NO_3)_2$, and $Co(NO_3)_2 \cdot 5H_2O$ (Alfa Aesar) in deionized water, mixed with citric acid in a 1:1 metal nitrate to citric acid molar ratio, adjusted to pH 6.5 with ammonium nitrate, and diluted with deionized water to 1 mol/L. Excess SSC solution was infiltrated into the scaffolds, and fired at 450°C for 0.5 hours to decompose the nitrates. The cells were infiltrated 8 times to about 20 vol% and finally fired at 800°C for 1 hour. A layer of $(La_{0.8}Sr_{0.2})_{0.98}MnO_3$ (LSM) ink was then screen printed and fired at 800°C for 1 hour as a current collector with a thickness of 10 μm. Silver metal grids were then applied as current collectors for electrochemical testing.

Pr_2NiO_4 infiltrated LSGM symmetric cell fabrication.—The cell fabrication method is similar to that described in Ref. 23. For the LSGM electrolyte, LSGM was first synthesized via solid state reaction. LSGM powder was synthesized from stoichiometric amounts of $SrCO_3$ (Sigma), La_2O_3 (Sigma), Ga_2O_3 (Sigma), and MgO (Alfa Aesar), which were ball milled for 24 hours in ethanol, dried, and then reacted at 1250°C for 12 hours. This LSGM powder was then ball milled in ethanol and 2 wt% polyvinyl butyral (Aldrich) binder, dried, and pressed into 0.5 g 19 mm diameter pellets. The green bodies were then sintered at 1450°C for 4 hours. LSGM scaffolds were screen printed onto the electrolyte pellets using an ink composed of commercially available LSGM (Praxair), Heraeus 737 vehicle, and 30 wt% of KS4 graphite flakes (Timrex) as pore former. Four screen printed layers were applied to each side, then heated to 600°C for one hour to burn away the pore former, and then fired at 1200°C for 4 hours to form a porous scaffold layer with interconnected LSGM particles 1–3 μm in size. A current collector was then applied on each scaffold by screen printing one layer of an $(La_{0.6}Sr_{0.4})(Co_{0.8}Fe_{0.2})O_{3-\delta}$ ink consisting of the same vehicle, pore former, and LSCF powder (Praxair). The entire assembly was then fired at 1100°C for one hour to produce a suitably porous current collector that was also well bonded to the scaffold. The resulting scaffold thickness was ∼ 40 μm and the LSCF layer was ∼ 10 μm thick with an area of 0.5 cm^2. The cathode infiltrate was a 2 mol/L nitrate solution prepared by dissolving stoichiometric amounts of $Pr(NO_2)_3 \bullet 6H_2O$ (Aldrich) and $Ni(NO_2)_3 \bullet 3H_2O$ (Fischer) in water and subsequently adding 0.06 mol of Triton X-100 (VWR). This solution was stirred for 24 hours to ensure good mixing. Each scaffold was infiltrated with this solution using excess fluid (∼6 μL) and removing the excess after allowing solution to infiltrate the porous scaffold for 5 minutes. The infiltrate was decomposed by heating to 450°C for 0.5 hours, leaving oxides of the respective metal ions. After 12 infiltrations, the symmetric cells were fired at 1000°C for 4 hours to form Pr_2NiO_4. Silver metal grids current collectors were applied for electrochemical testing.

Pressurized electrochemical impedance spectroscopy (EIS) and analysis.—A custom designed pressure system (Deltech Furnaces Inc, Denver, CO) was used to collect EIS data. The system is capable of reaching pressures up to 11 atmospheres, and temperatures up to 850°C. Details of the system geometry and controls are described elsewhere.[24] The single-phases NNO/LSGM and LSCF/GDC symmetric cells were operated at 700°C and the two-phases infiltrated PNO-LSGM and SSC-GDC symmetric cells were operated at 550°C for the entire measured pressure range. EIS data was collected for a range of oxygen pressures for all cells from 0.2 bar to 10 bar. Below 1 bar oxygen, the total pressure in the system remains at 1 bar and is balanced with nitrogen with a total flow rate of 40 sccm. EIS data was collected in the frequency range 0.1–10^6 Hz using a Zahner IM6 impedance spectrometer.

Equivalent circuit model fitting was performed using Matlab and Excel software[25] in order to obtain the most accurate possible R_p values from the data. The circuit models used for the infiltrated electrodes were either (L-R-RQ) or (L-R-RQ-RQ), where L is an inductance, R is a resistance, and RQ represents a constant phase element. The circuit model used for powder electrodes cells was (L-R-G in Boukamp notation), where G represents a modified Gerischer element that accounts for the distribution of relaxation times.[26] The inductor accounts for inductance in the wire leads through the system, the resistor represents the electrolyte resistance, and the Gerischer element represents the impedance associated with the co-limiting oxygen surface exchange and diffusion processes in the porous MIEC electrode, as described in the ALS model.[27] Other contributions to the polarization resistance (such as gas diffusion) were found to be negligible.

Results

Figure 1 shows the Nyquist and Bode plots of the EIS spectra taken at 550°C from infiltrated SSC-GDC electrode cells at selected pO_2 values. Figure 2 shows the same for infiltrated PNO-LSGM electrode cells. Both electrodes have relatively low polarization resistance R_P, given the relatively low operating temperature, that is

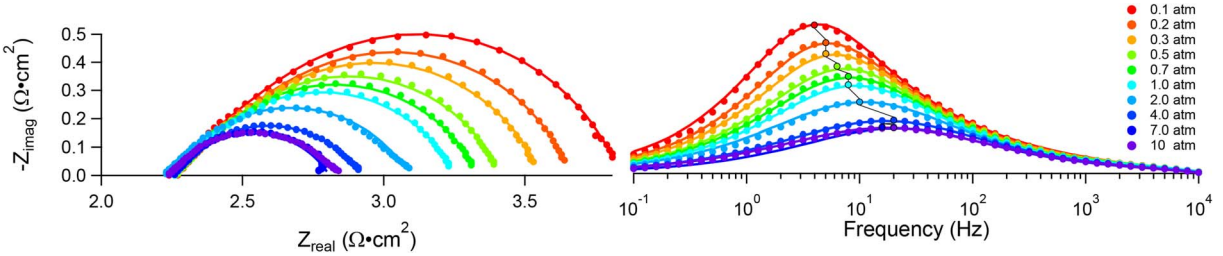

Figure 2. Nyquist and Bode plots as a function of oxygen pressure at 550°C for Pr_2NiO_4 infiltrated into LSGM. The resistance values are taken from fits using a general (L-R-RQ-RQ) circuit. Fits are displayed as solid lines on the plots and the maximum frequency is outlined on the Bode plot.

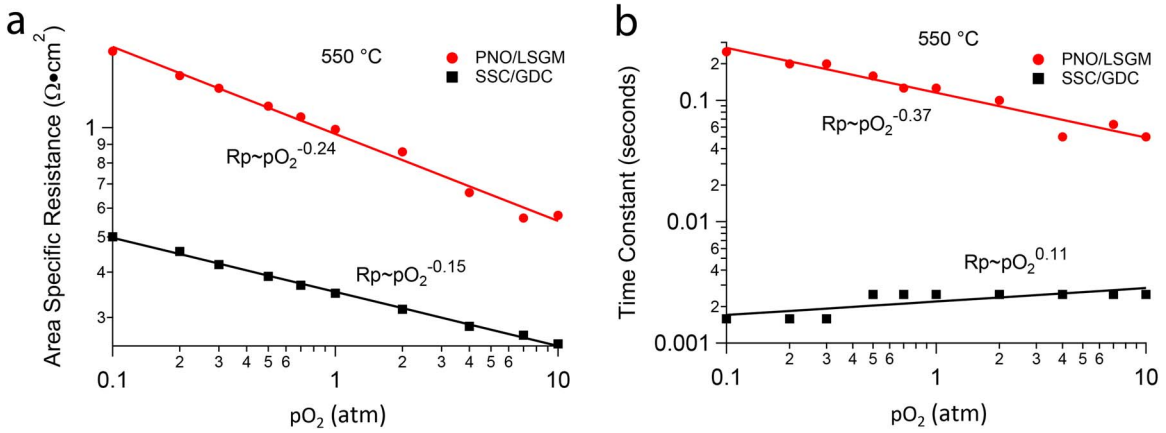

Figure 3. a) Polarization resistance as a function of oxygen pressure at 550°C for PNO-LSGM and SSC-GDC. The resistance values are taken from fits in Figures 1 and 2. b) Time constants as a function of oxygen pressure at 550°C for PNO-LSGM and SSC-GDC. The time constants are the inverse of the peak frequency.

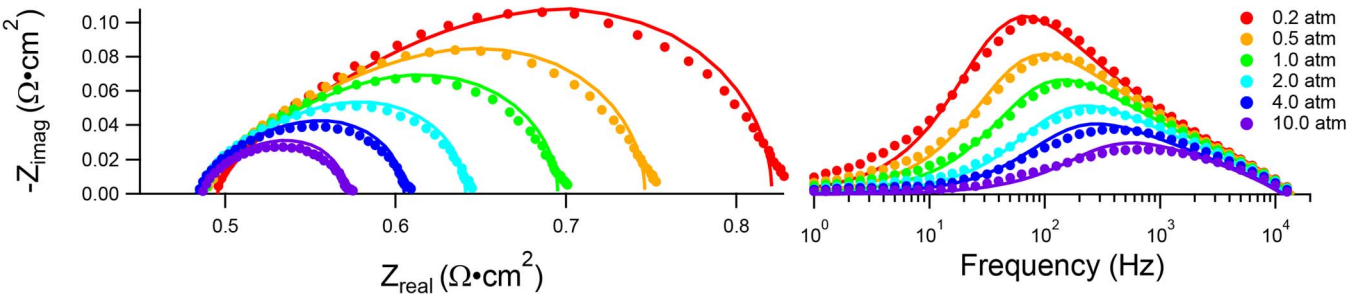

Figure 4. Bode and Nyquist plots of an NNO symmetric cell at 700°C in the pressure range from 0.2 to 10 bar pO_2. Solid lines are (L-R-G) equivalent circuit fits.

further decreased with increasing pO_2. The arcs are depressed and reasonably symmetric. The PNO-LSGM electrode arcs had peak frequencies that increased with increasing pO_2, i.e., with decreasing R_P, - the normal dependence observed if the electrode capacitance remains approximately constant. The SSC-GDC electrode showed the reverse trend of peak frequency with pO_2, suggesting a substantial increase in capacitance with increasing pO_2.

Figure 3a shows the polarization resistance R_P of infiltrated SSC-GDC and PNO-LSGM electrode cells, derived best fits to EIS data such as that shown in Figures 1 and 2, as a function of oxygen pressure. R_P for the PNO infiltrated electrode has a stronger power-law dependence, ${pO_2}^{-0.24}$, than that for the SSC infiltrated electrode, ${pO_2}^{-0.15}$. Figure 3b shows the dependences of the time constant (taken as the inverse of the peak frequency) for the two electrodes. The time constants show opposite trends with pO_2: increasing slightly in SSC-GDC as ${pO_2}^{0.11}$ and decreasing as ${pO_2}^{-0.37}$ in PNO-LSGM.

Figure 4 shows EIS data at selected pO_2 values for a Nd_2NiO_4-electrode symmetric cell. Figure 5 shows EIS data at selected pO_2 values for an LSCF symmetric cell. For both cells, the characteristic frequency of the dominant process shifts to higher frequencies with increasing pO_2, as R_P decreases, but the shift is greater for LSCF. Fitting was done using a single Gerischer element, where the complex resistance (Z_G) is defined:

$$Z_G = R_G\sqrt{\frac{1}{1+j\omega t_G}} \qquad [1]$$

where R_G and t_G are measured from the EIS fit, ω is angular frequency, and j is the imaginary number. The fits are reasonably good for most pO_2 values, suggesting that the ALS model, where the electrode process is co-limited by surface exchange and diffusion processes, should provide a reasonable representation. This agrees with previous studies performed in the low pO_2 range below 1 atm.[20,27] The deviations from a perfect Gerischer shape may indicate slight deviations from the ALS model, perhaps due to the electrode utilization length becoming either too large (comparable to the electrode thickness) or too small (comparable to the electrode feature size).[20,27] Since there is only one element fitting the electrode polarization response (the response at $>10^4$ Hz is attributed to the electrolyte), the fitted Gerischer resistance gives the total electrode polarization resistance, i.e., $R_P = R_G$.

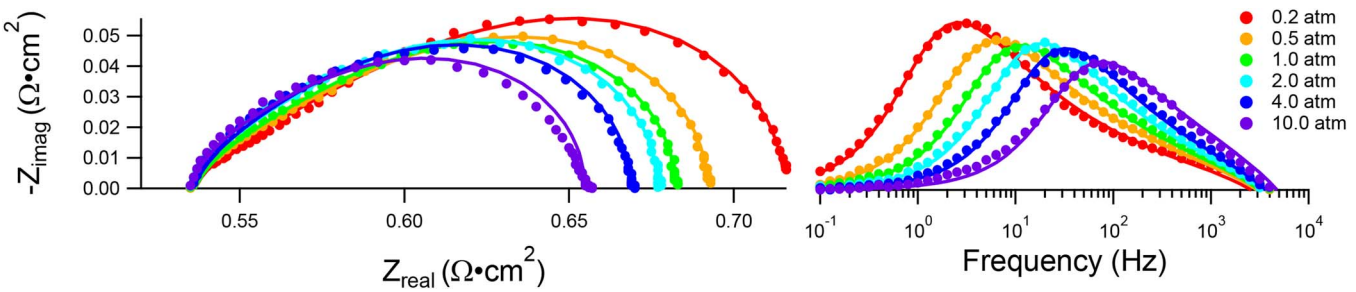

Figure 5. Bode and Nyquist plots of an LSCF symmetric cell at 700°C in the pressure range from 0.2 to 10 bar pO_2. Solid lines are (L-R-G) equivalent circuit fits.

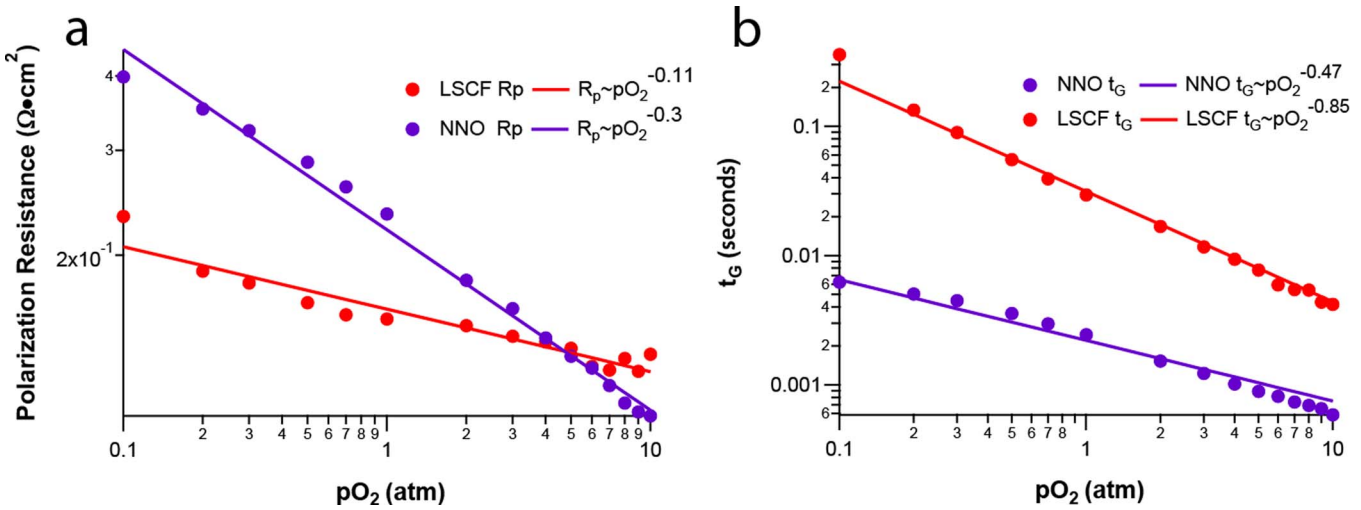

Figure 6. a) Polarization resistance versus pO_2 for LSCF and NNO at 700°C. Data points are taken from L-R-G circuit models fits to the EIS data, and solid lines indicate power law fits. b) t_G values obtained from the fits versus pO_2 for LSCF and NNO at 700°C.

Figure 6a plots the pO_2–dependence of the Gerischer resistance R_G for the NNO and LSCF symmetric cells, obtained by fitting the EIS data at 700°C as shown in Figs. 4 and 5. The data are fit reasonably well by a $pO_2^{-0.30}$ dependence for NNO and $pO_2^{-0.11}$ for LSCF, as shown. Figure 6b shows the t_G values obtained from the fits; the time constant values, the inverse of the peak frequencies discussed above, decrease with increasing pO_2.

Discussion

The above results show a significant difference in the pO_2 dependences of electrode polarization resistance for nickelate versus perovskite electrodes. The difference is observed for two different nickelate and perovskite compositions, and for different electrode structures – single phase porous electrodes and electrodes formed by infiltration of the MIEC into a porous ion conducting scaffold. This suggests that the different pO_2 dependence arise from an inherent difference between perovskite and nickelate MIECs. We propose that this is related to the different dominant ionic-charge carrier types – oxygen vacancies in perovskites and oxygen interstitials in nickelates. In particular, oxygen pressurization is expected to reduce the oxygen vacancy concentration, which are the O-ion charge carriers in a perovskite, degrading its ability to transport oxygen ions, and mitigating the performance improvement expected because of the increased pO_2. On the other hand, pressurization is expected to increase the oxygen interstitial concentration, responsible of the O-ion transport at the nickelates, improving oxygen ion transport and leading to a larger performance improvement. The differences between the pO_2 dependences are less for the infiltrated electrodes, perhaps because the ionically-conducting scaffold has a constant oxygen vacancy concentration that provides fast oxygen transport regardless of the pO_2. In this case, the changes in MIEC defect concentration with pressure affect only the surface exchange process.

In the following, the ALS model[20,27] is applied in an attempt to test the above hypothesis and quantify the defect concentration variations with pO_2. As noted above, the ALS model used here requires that the utilization length be much smaller than the electrode thickness and much larger than the electrode feature size;[20,27,28] this criterion will be checked below. The ALS model predicts the Gerischer response shown in Eq. 1 with t_G given by:

$$t_G = \frac{(1-\epsilon)\, c_o x_\delta^0}{4 a R_0 A_0} \qquad [2]$$

and R_G given by

$$R_G = \frac{RT}{4F^2}\sqrt{\frac{\tau}{4a\,(1-\epsilon)\,R_o c_0 x_\delta^0 D}} \qquad [3]$$

Where ε is the electrode porosity, a is the internal specific surface area of the solid phase, τ is the tortuosity of the solid phase, c_0 is the concentration of oxygen sites involved in diffusion, $x_\delta{}^0$ is the molar fraction of interstitial or vacancy defects at equilibrium, A_0 is the thermodynamic factor, D is the oxygen diffusivity, and R_0 is the molar surface exchange rate defined as:

$$R_o = \frac{k_{chem}}{A_0}(pO_2)^{0.5} c_0 \qquad [4]$$

Here, k_{chem} is the surface exchange coefficient and relates to k_δ and k^* as:

$$k_\delta = \frac{k^*}{x_\delta^0} = \frac{k_{chem}}{A_0} \qquad [5]$$

Where k_δ and k^* refer to the normalized and isotope exchange derived surface exchange values.[20]

Similarly,

$$D_\delta = \frac{D^*}{x_\delta^0} = \frac{D_{chem}}{A_0} \qquad [6]$$

Where D_δ and D^* refer to the normalized and isotope exchange derived oxygen diffusion coefficients.

Substitution of Eq. 4 into Eq. 3 yields

$$R_G = \frac{RT}{4F^2}\sqrt{\frac{\tau A_0^2}{4a\,(1-\epsilon)\,k_{chem} c_0^2 x_\delta^0 D_{chem}}}(pO_2)^{-0.25} \qquad [7]$$

Note that if all the terms in Eq. 7 were independent of pO_2, then $R_G \propto pO_2^{-0.25}$, as compared to the fits at $pO_2^{-0.11}$ for LSCF and $pO_2^{-0.30}$ for NNO shown in Figure 6. The thermodynamic factor A_0 is a function of oxygen chemical potential,

$$A_0 = \pm\frac{1}{2RT}\left(\frac{\partial \mu_{O_2}}{\partial \ln\left(x_\delta^0\right)}\right) = \pm\frac{1}{2}\left(\frac{\partial \ln(pO_2)}{\partial \ln\left(x_\delta^0\right)}\right) \qquad [8]$$

the (−) sign corresponds to O-vacancies and (+) to O-interstitials. A_0 can often be assumed constant with reasonable accuracy over the measured pO_2 range at low non-stoichiometric values.[17] Furthermore, k_{chem} and D_{chem} should be independent of pO_2.[20,29] The only other term in Eq. 7 that might be expected to vary with pO_2 is the oxygen non-stoichiometry x_δ^0. Thus, the observed deviations of measured R_G from the $pO_2^{-0.25}$ dependence can be explained by variations in x_δ^0.

An expression for x_δ^0 can be obtained by rearranging Eq. 7:

$$x_\delta^0 = \frac{R^2T^2\tau A_0^2}{64F^4R_G^2a\,(1-\epsilon)\,c_0^2k_{chem}D_{chem}}(pO_2)^{-0.5} \quad [9]$$

That is, the non-stoichiometry can be obtained from the R_G data, if the electrode material parameters A_0, c_0, k_{chem}, and D_{chem} are known along with the microstructural parameters a, ε, and τ. Alternatively, plugging Eq. 4 into Eq. 2 and re-arranging yields:

$$x_\delta^0 = \frac{4at_Gk_{chem}(pO_2)^{0.5}}{1-\epsilon} \quad [10]$$

Thus, the non-stoichiometry can also be determined from t_G data if select materials and microstructural parameters are known. Using Eq. 9 with the measured R_G values yields x_δ^0 values for each pO_2, but substitution in Eq. 2 yields poor agreement with measured t_G values. Similarly, using Eq. 10 with the measured t_G values yields a set of x_δ^0 values, but substitution in Eq. 7 yields poor agreement with measured R_G values. These disagreements could arise in part from the wide variations in literature k_{chem}. In order to obtain a set of x_δ^0 values that provide a good match to both the R_G and t_G values versus pO_2, a combined expression, obtained by multiplying Equations 9 and 10, was used:

$$x_\delta^0 = \frac{RTA_0}{4F^2R_G\,(1-\epsilon)\,c_0}\sqrt{\frac{t_G\tau}{D_{chem}}} \quad [11]$$

Note that both R_G and t_G appear in Eq. 11, and the terms a, k_{chem}, and $(pO_2)^{0.5}$ are eliminated in the combined expression.

The molar fraction of vacancies or interstitials is obtained from Eq. 11 for each pO_2 using the measured t_G and R_G values, τ and ε measured for each particular electrode microstructure,[19,20] and literature values of $D_{chem} = 6.0 \times 10^{-6}$ cm^2/s for LSCF[30] and 2.9×10^{-7} cm^2/s for NNO.[20] The NNO oxygen interstitial concentration in Figure 7a increases slowly with increasing pO_2, and is fit reasonably well by the power law $pO_2^{0.03}$. This slope appears to be in good agreement with changes in x_δ^0 with pO_2 measured at ≤ 1 atm, also shown in the figure. The LSCF oxygen vacancy concentration x_δ^0 in Figure 7b decreases with increasing pO_2, fitting to the power law $pO_2^{-0.35}$. This slope is in fair agreement with the variation in vacancy concentrations, for ≤ 1 atm, from Ref. 27. As shown in Table I, there are different reported D_{chem} values, but their spread is relatively small. We have simply chosen the value that provides a better match to literature x_δ^0 values. Note that the calculated x_δ^0 values will shift slightly with the D_{chem} value chosen, but the slope with pO_2 will not. That is, the trends shown in Figures 7a and 7b are valid, even if the absolute values may have some error. Note that the A_0 values used in Eq. 11 are obtained directly from the slopes in these figures, as per Eq. 8, yielding 1.417 for LSCF and 14.47 for NNO.

Table I. Oxygen diffusion and surface exchange coefficients for LSCF and NNO.

LSCF D at 700°C (cm^2/s)		NNO D at 700°C (cm^2/s)	
D_{chem}[34]	2.04×10^{-6}	D^*[35]	3.0×10^{-8}
D_{chem}[30]	6.03×10^{-6}	D_δ[20]	2.0×10^{-8}
D^*[19]	5.27×10^{-10}		
LSCF k at 700°C (cm/s)		**NNO k at 700°C (cm/s)**	
k_{chem}[19]	9.56×10^{-5}	k_{chem}[20]	1.82×10^{-4}
k_{chem}[28]	1.05×10^{-5}	k_{chem}[35]	8.00×10^{-5}
k_{chem}[36]	1.04×10^{-6}	k_{chem} (this work)	1.21×10^{-4}
k_{chem} (this work)	3.83×10^{-6}		

The match between the measured and calculated R_G and t_G values, based on the above x_δ^0 dependences, is shown for NNO in Figure 8, and for LSCF in Figure 9. Note that calculation of these values using Eqs. 7 and 2, respectively, requires values of k_{chem}. However, as mentioned earlier, there is a wide variation in reported k_{chem} values, making it difficult to choose a representative value. Thus, k_{chem} is used as a constant fitting parameter here to match the R_G and t_G data in Figures 8 and 9. Table I shows that the k_{chem} values obtained – 3.83×10^{-6} (cm/s) for LSCF and 1.21×10^{-4} (cm/s) for NNO – are well within the range of values reported in the literature. There is generally good agreement with the experimental data shown in the figures (the only significant deviation is at 0.1 atm), verifying that Eq. 11 yields x_δ^0 values that are consistent with the measured data. That is, the change in the concentration of these defects can explain the different dependences of the measured R_G and t_G on pO_2, for both NNO and LSCF. For NNO, R_G decreases slightly faster than the $pO_2^{-0.25}$ dependence shown in Eq. 7, because the interstitial content increases modestly. For LSCF, R_G decreases much slower than $pO_2^{-0.25}$ because the vacancy content decreases substantially.

As noted earlier, the ALS model is only valid for reasonable utilization lengths, i.e., the electrode lengths over which significant oxygen exchange and diffusion occurs, which can be calculated using:

$$l_\delta = \sqrt{\frac{(1-\epsilon)\,D_\delta c_0 x_\delta^0}{4a\tau R_0}} \quad [12]$$

Using the above values, the utilization length for LSCF is found to range from 15.4 to 2.1 microns over the 0.1 to 10 atm pressure range. Utilization lengths in NNO were smaller, varying from 396 nm to 134 nm over the same range. The utilization lengths being smaller than the electrode thickness ~20 microns indicates that the electrodes satisfy the thick electrode assumption to be analyzed by the ALS model.

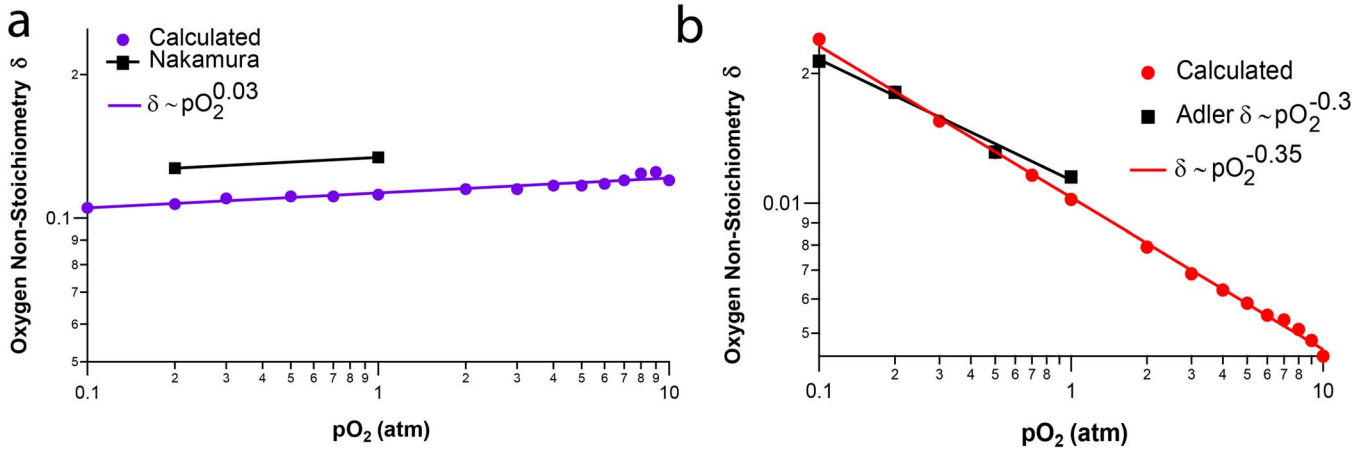

Figure 7. Oxygen non-stoichiometry δ versus oxygen pressure for $Nd_2NiO_{4+\delta}$ (a) and $La_{0.6}Sr_{0.4}Co_{0.2}F_{0.8}O_{3-\delta}$ (b) at 700°C. Literature values for oxygen non-stoichiometry values are displayed in black.[18,27]

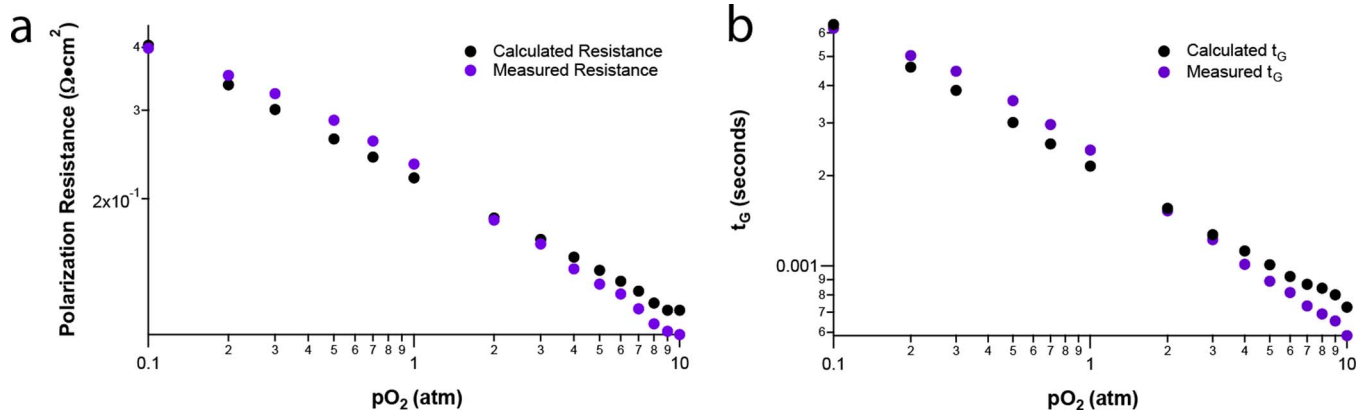

Figure 8. a) Measured polarization resistance versus pO_2 for Nd_2NiO_4 compared to values calculated from derived x_δ^0 b) Measured and calculated time constants versus pO_2.

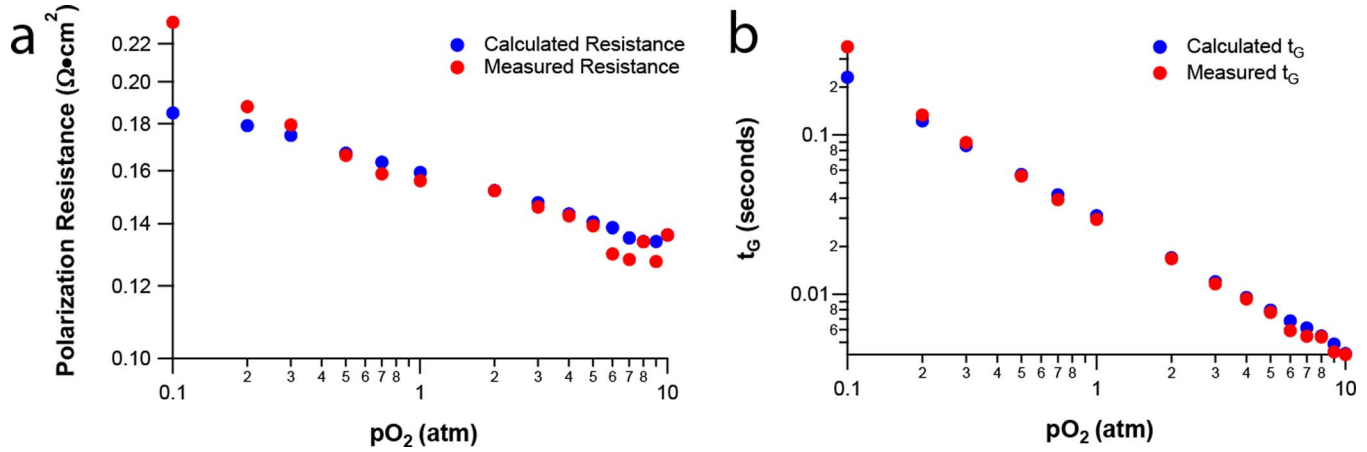

Figure 9. a) Measured polarization resistance versus pO_2 for LSCF compared to values calculated from derived x_δ^0 b) Measured and calculated time constants versus pO_2.

However, the NNO electrode utilization length is comparable to the electrode particle size.

The above analysis using the ALS model is applicable to the porous single-phase electrodes. Although a defect concentration analysis was not done for the more complicated infiltrated composite SSC and PNO electrodes in this study, similar trends with pO_2 are observed. In analyzing the infiltrated composites, it should be considered that they contain ionic conductors (GDC or LSGM) with oxygen defect concentrations that, unlike the MIECs, do not vary with pO_2. This probably explains why the difference in the pO_2 dependences for SSC and PNO is smaller than for the single-phase electrodes.

While there is little other data available for MIEC electrodes under pressurized conditions, data for $pO_2 \leq 1$ atm generally supports the present trends. That is, the perovskites show weaker x_δ^0 dependences on pO_2, e.g., m ~ -0.13 for LSCF at 750°C[31] and m ~ -0.17–0.22 for LSC at various temperatures,[29] whereas nickelates show stronger pO_2 dependence, e.g., m $\sim$ 0.25–0.5 for NNO at various temperatures.[20,32,33] The unique feature of the present results is to demonstrate that these trends continue to pO_2 values up to 10 atm.

Conclusions

The polarization resistances of nickelate (NNO and PNO) electrodes were found to decrease more rapidly with increasing oxygen partial pressure up to 10 atm, than perovskite (LSCF and SSC) electrodes. The differences were explained based on the different oxygen defect types – the oxygen interstitial concentration in the nickelate electrodes increased with increasing pO_2, whereas the oxygen vacancy concentration in the perovskites decreased. The different dependencies of R_P on pO_2 for single-phase porous NNO and LSCF electrodes were explained quantitatively by the ALS model for reasonable variations of interstitial and vacancy concentrations. The infiltrated composite nickelate (PNO) and perovskite (SSC) electrodes showed a similar effect, although there was less difference between their R_P dependences. Thus, if nickelate and perovskite electrodes shown similar R_P under ambient air, the nickelate electrode can be expected to provide lower R_P under pressurized conditions.

Acknowledgments

The authors gratefully acknowledge financial support by NSF OISE grant # 1545907, Global Climate and Energy Project (Stanford University) award #51922, and a Northwestern University McCormick School of Engineering Catalyst Award.

References

1. S. H. Jensen, X. F. Sun, S. D. Ebbesen, R. Knibbe, and M. Mogensen, *International Journal of Hydrogen Energy*, **35**(18), 9544 (2010).
2. S. H. Jensen, X. Sun, S. D. Ebbesen, and M. Chen, *Fuel Cells*, **16**(2), 205 (2016).
3. S. C. Singhal, *Solid State Ionics*, **135**(1–4), 305 (2000).
4. D. M. Bierschenk, J. R. Wilson, and S. A. Barnett, *Energ Environ Sci*, **4**(3), 944 (2011).
5. S. H. Jensen, C. Graves, M. Mogensen, C. Wendel, R. Braun, G. Hughes, Z. Gao, and S. A. Barnett, *Energ Environ Sci*, **8**(8), 2471 (2015).
6. W. J. Yang, S. K. Park, T. S. Kim, J. H. Kim, J. L. Sohn, and S. T. Ro, *J. Power Sources*, **160**(1), 462 (2006).
7. W. Burbank, D. D. Witmer, and F. Holcomb, *J. Power Sources*, **193**(2), 656 (2009).

8. R. J. Braun and P. Kazempoor, in *Solid Oxide Fuel Cells: From Materials to System Modeling*, M. Ni and T. S. Zhao, eds., p. 327–382, Royal Soc Chemistry, Cambridge, (2013).
9. X. Sun, M. Chen, S. H. Jensen, S. D. Ebbesen, C. Graves, and M. Mogensen, *International Journal of Hydrogen Energy*, **37**(22), 17101 (2012).
10. D. M. Bierschenk, J. R. Wilson, E. Miller, E. Dutton, and S. A. Barnett, *Ecs Transactions*, **35**(1), 2969 (2011).
11. P. Kazempoor and R. J. Braun, *International Journal of Hydrogen Energy*, **39**(11), 5955 (2014).
12. C. Drevet, M. Henault, and J. Fouletier, *Solid State Ionics*, **136**, 807 (2000).
13. T. Matsui, M. Futamura, R. Kikuchi, and K. Eguchi, in *Solid Oxide Fuel Cells 10*, K. Eguchi, S. C. Singhai, H. Yokokawa, and H. Mizusaki, eds., Vol. **7**, p. 851–858, Electrochemical Society Inc, Pennington, (2007).
14. L. Zhou, M. J. Cheng, B. L. Yi, Y. L. Dong, Y. Cong, and W. S. Yang, *Electrochim. Acta*, **53**(16), 5195 (2008).
15. E. C. Thomsen, G. W. Coffey, L. R. Pederson, and O. A. Marina, *J. Power Sources*, **191**(2), 217 (2009).
16. Z. Gao, L. V. Mogni, E. C. Miller, J. G. Railsback, and S. A. Barnett, *Energ Environ Sci*, **9**(5), 1602 (2016).
17. M. H. R. Lankhorst and J. E. tenElshof, *J Solid State Chem*, **130**(2), 302 (1997).
18. T. Nakamura, K. Yashiro, K. Sato, and J. Mizusaki, *J Solid State Chem*, **182**(6), 1533 (2009).
19. H. Q. Wang, K. J. Yakal-Kremski, T. Yeh, G. M. Rupp, A. Limbeck, J. Fleig, and S. A. Barnett, *J Electrochem Soc*, **163**(6), F581 (2016).
20. K. Yakal-Kremski, L. V. Mogni, A. Montenegro-Hernandez, A. Caneiro, and S. A. Barnett, *J Electrochem Soc*, **161**(14), F1366 (2014).
21. A. Montenegro-Hernandez, J. Vega-Castillo, L. Mogni, and A. Caneiro, *International Journal of Hydrogen Energy*, **36**(24), 15704 (2011).
22. A. V. Call, J. G. Railsback, H. Q. Wang, and S. A. Barnett, *Phys Chem Chem Phys*, **18**(19), 13216 (2016).
23. J. G. Railsback, Z. Gao, and S. A. Barnett, *Solid State Ionics*, **274**, 134 (2015).
24. G. Hughes, J. Railsback, D. Butts, and S. A. Barnett, *Ecs Transactions*, **68**(1), 687 (2015).
25. J.-L. Dellis, 2014.
26. B. L. G. J.-P. Diard and C. Montella. Bio-Logic SAS Instruments, 2013.
27. S. B. Adler, J. A. Lane, and B. C. H. Steele, *J Electrochem Soc*, **143**(11), 3554 (1996).
28. C. Endler-Schuck, J. Joos, C. Niedrig, A. Weber, and E. Ivers-Tiffee, *Solid State Ionics*, **269**, 67 (2015).
29. Y. X. Lu, C. Kreller, and S. B. Adler, *J Electrochem Soc*, **156**(4), B513 (2009).
30. P. Ried, E. Bucher, W. Preis, W. Sitte, and P. Holtappels, *Solid Oxide Fuel Cells 10 (Sofc-X), Pts 1 and 2*, **7**(1), 1217 (2007).
31. E. P. Murray, M. J. Sever, and S. A. Barnett, *Solid State Ionics*, **148**, 27 (2002).
32. F. Mauvy, C. Lalanne, J. M. Bassat, J. C. Grenier, H. Zhao, L. H. Huo, and P. Stevens, *J Electrochem Soc*, **153**(8), A1547 (2006).
33. M. J. Escudero, A. Aguadero, J. A. Alonso, and L. Daza, *J Electroanal Chem*, **611**(1–2), 107 (2007).
34. H. J. M. Bouwmeester, M. W. Den Otter, and B. A. Boukamp, *J Solid State Electr*, **8**(9), 599 (2004).
35. E. Boehm, J. M. Bassat, P. Dordor, F. Mauvy, J. C. Grenier, and P. Stevens, *Solid State Ionics*, **176**(37-38), 2717 (2005).
36. A. Esquirol, N. P. Brandon, J. A. Kilner, and M. Mogensen, *J Electrochem Soc*, **151**(11), A1847 (2004).